

Vortex-ring quantum droplets in a radially-periodic potential

Bin Liu^{1,2}, Yi xi Chen¹, Ao wei Yang¹, Xiao yan Cai¹, Yan Liu³, Zhi huan Luo³,
Xi zhou Qin^{1,2}, Xun da Jiang^{1,2},* Yong yao Li^{1,2}, and Boris A. Malomed^{4,5}
¹*School of Physics and Optoelectronic Engineering, Foshan University, Foshan 528000, China*
²*Guangdong-Hong Kong-Macao Joint Laboratory for Intelligent Micro-Nano
Optoelectronic Technology, Foshan University, Foshan 528000, China*
³*Department of Applied Physics, College of Electronic Engineering,
South China Agricultural University, Guangzhou 510642, China*
⁴*Department of Physical Electronics, School of Electrical Engineering, Faculty of Engineering,
and Center for Light-Matter Interaction, Tel Aviv University, Tel Aviv 69978, Israel and*
⁵*Instituto de Alta Investigación, Universidad de Tarapacá, Casilla 7D, Arica, Chile*

We establish stability and characteristics of two-dimensional (2D) vortex ring-shaped quantum droplets (QDs) formed by binary Bose-Einstein condensates (BECs). The system is modeled by the Gross-Pitaevskii (GP) equation with the cubic term multiplied by a logarithmic factor (as produced by the Lee-Huang-Yang correction to the mean-field theory) and a potential which is a periodic function of the radial coordinate. Narrow vortex rings with high values of the topological charge, trapped in particular circular troughs of the radial potential, are produced. These results suggest an experimentally relevant method for the creation of vortical QDs (thus far, only zero-vorticity ones have been reported). The 2D GP equation for the narrow rings is approximately reduced to the 1D form, which makes it possible to study the modulational stability of the rings against azimuthal perturbations. Full stability areas are delineated for these modes. The trapping capacity of the circular troughs is identified for the vortex rings with different winding numbers (WNs). Stable compound states in the form of mutually nested concentric multiple rings are constructed too, including ones with opposite signs of the WN. Other robust compound states combine a modulationally stable narrow ring in one circular potential trough and an azimuthal soliton performing orbital motion in an adjacent one. The results may be used to design a device employing coexisting ring-shaped modes with different WN for data storage.

I. INTRODUCTION

Quantum droplets (QDs) were predicted, as a new species of quantum matter, by Petrov and Astrakharchik [1, 2], and then promptly created in dipolar [3, 4] and binary bosonic gases, both homoatomic [5–7] and heteroatomic [8] ones. The QDs are maintained by the balance of the effective mean-field attraction (which itself is a result of the competition of the inter-component attraction and intra-component self-repulsion), driving the system towards the collapse, and the higher-order self-repulsion in each component induced by quantum fluctuations, which is represented by the Lee-Huang-Yang (LHY) correction [9] to the respective Gross-Pitaevskii (GP) equations. This correction takes different forms in 3D, 2D and 1D versions of the GP equations (in particular, its sign flips into effective self-attraction in 1D) [2, 10, 11].

QDs have drawn much interest as stable self-trapped modes, both multidimensional and one-dimensional [12–51]. In addition to their significance to fundamental studies, they offer potential applications, such as the design of matter-wave interferometers [52].

A remarkable result is the prediction of the fact that QDs with embedded vorticity (topological charge, alias winding number, WN), $S \geq 1$, may also be stable, in the 2D [53] and 3D [54] settings alike. These are essential findings, as the stability is a major issue for fundamental and vortical multidimensional soliton-like states [51, 55]. Stable semidiscrete vortex QDs were also predicted in arrays of coupled 1D cigar-shaped traps [56].

However, the creation of vortex QDs in an experiment has not been reported yet, and it is considered as a technically challenging objective. Therefore, search for settings which facilitate the existence of such stable topological modes is a relevant problem. A known possibility for that is offered by the use of spatially periodic [57, 58] or quasiperiodic [59] lattice potentials. It was predicted that they not only stabilize vortex modes with various degrees of complexity [60–62], but also alter formation patterns in many ways [63–89]. In 1D settings with periodic potentials, QDs were studied too [90, 91]. Vortex QDs with $S = 1$ in the 2D setting including the square-lattice potential were considered in Ref. [92]. On the other hand, because the square lattice breaks the rotational symmetry and conservation of

*Electronic address: jxd194911@163.com

the angular momentum, it is more natural to use radial (axisymmetric) lattices as an experimentally relevant means supporting stable self-trapped vortex modes, especially ones with high WN values. In particular, Ref. [93] reported stable vortex solitons with $S = 11$ maintained by the radial lattice in the dipolar Bose-Einstein condensate (BEC) with repulsive long-range dipole-dipole interactions.

The objective of this work is to demonstrate that stable 2D vortex QDs, which are formed by binary BECs with contact (rather than long-range) interactions, can be effectively made and controlled with the help of a radially periodic axisymmetric potential, which directly suggests a new approach for the creation of vortex QDs in experiments. The system is modeled by the GP equation with this potential and LHY term. The respective vortex QDs are ring-shaped, being trapped in particular circular troughs of the radial potential with multiple minima, cf. Refs. [77, 94, 95]. The difference from the above-mentioned stable self-trapped vortex states in the free space is that those ones may not be stable unless they are very broad [53] (which is an obvious difficulty for the creation of such modes in the experiment), while it is shown below that the axisymmetric lattice potential may support narrow vortex rings as stable modes, thus offering an advantage for the experimental realization. For narrow rings, the 2D GP equation is approximately reduced to its 1D form by eliminating the radial coordinate. The modulational stability of the rings in the azimuthal direction is then analyzed in the framework of the 1D equation. Effects of the depth and period of the radial potential on the vortex ring-shaped QDs in the full 2D form are systematically studied by means of numerical methods, and stability areas are identified for them. Composite vortex patterns, built of concentric rings nested in different circular troughs, which carry different WNs, including the case when a vortex ring is embedded in a larger one with the opposite sign of the WN, are considered too (while stationary multi-ring patterns do not exist in the free space). Earlier, multi-ring concentric patterns with different WNs in different rings were introduced in Ref. [96] as solutions to the 2D complex Ginzburg-Landau equation with the cubic-quintic nonlinearity (without the radial potential); however, unlike the present setting, those patterns are dissipative ones. These results offer a possibility to design a new encoding device, using the coexisting rings with different WNs for storing different data components.

The rest of the paper is structured as follows. The model is introduced in Sec. II, and analytical results produced by the reduced 1D GP equation are presented in Sec. III. Numerical findings for the 2D vortex ring-shaped QDs are summarized in Sec. IV, and the multi-ring vortex QDs combining different WNs in concentric circular troughs are the subject of Sec. V. The work is concluded by Sec. VI.

II. THE MODEL

According to Ref. [53, 92], we assume that QDs, which are formed by the binary BEC, are strongly confined in the transverse direction, having a lateral size $l \gg \sqrt{a_{1,2}a_{\perp}}$, where $a_{1,2}$ and a_{\perp} are the scattering lengths accounting for the self-repulsion of each component and the transverse confinement length, respectively. This condition can be readily implemented in a typical experimental setup, with $a_{1,2} \sim 3$ nm, $a_{\perp} \lesssim 1$ μ m, and $l \sim 10$ μ m. Assuming the symmetry between the two components, i.e., $a_1 = a_2$, the system of coupled GP equations including the LHY correction is reduced to the scaled 2D form [2],

$$i \frac{\partial}{\partial t} \Psi_j = \left(-\frac{1}{2} \nabla^2 + V(r) + \frac{\delta E_{2D}}{\delta n_j} \right) \Psi_j, \quad (1)$$

where $j = 1, 2$ are labels for the two species with wave functions Ψ_j and densities $n_j = |\Psi_j|^2$, $\nabla^2 = \partial_r^2 + r^{-1} \partial_r + r^{-2} \partial_{\theta}^2$ is the Laplacian written in the polar coordinates, and $V(r)$ is the radial potential. The total potential energy E_{2D} of the system includes the mean-field and LHY terms, *viz.*,

$$E_{2D} = \frac{1}{2} \int_0^{\infty} r dr \int_0^{2\pi} d\theta \left[g(n_1 - n_2)^2 + (n_1 + n_2)^2 \ln \left(\frac{n_1 + n_2}{\sqrt{e}} \right) \right], \quad (2)$$

where g is the mean-field coupling constant [2]. In the symmetric state, with $\Psi_1 = \Psi_2 \equiv \Psi/\sqrt{2}$ and $n_1 = n_2 = n/2 \equiv |\Psi|^2/2$, the system of equations (1) amounts to a single LHY-corrected GP equation:

$$i \frac{\partial \Psi}{\partial t} = -\frac{1}{2} \nabla^2 \Psi + V(r) \Psi + \ln \left(|\Psi|^2 \right) \cdot |\Psi|^2 \Psi. \quad (3)$$

Note that the nonlinearity with the logarithmic factor in Eq. (3), $\ln n$, implies self-attraction at $n < 1$ and self-repulsion at $n > 1$, respectively.

Similar to Ref. [77], we choose the axisymmetric potential with depth $V_0 > 0$ (so that the origin at $r = 0$ represents a local maximum of the potential) and radial period D (with experimentally relevant values \sim a few μ m),

$$V(r) = V_0 \cos^2 \left(\frac{\pi}{D} r \right), \quad (4)$$

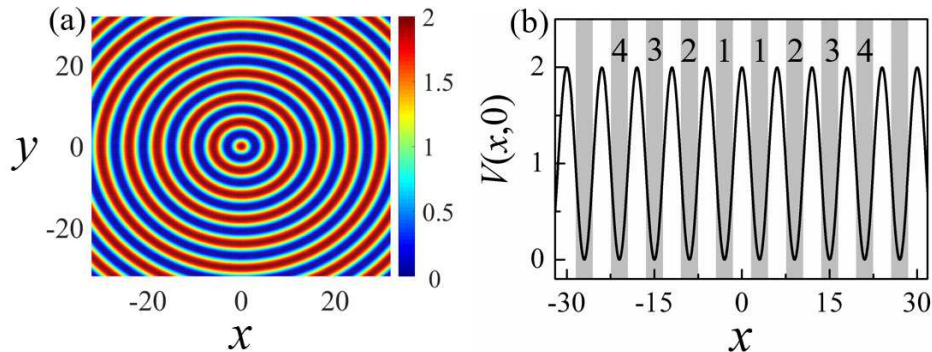


FIG. 1: (Color online) (a) The radially periodically potential (4) with $V_0 = 2$. (b) Its cross section, $V(x, 0)$, along $y = 0$. In the latter panel, numbers 1, 2, 3, ... represent integer values O_n in Eq. (9).

see Fig. 1(a). This potential can be created by a cylindrical laser beam passed through an appropriate amplitude-modulation plate. An essential property of the potential with multiple concentric troughs is that ring-shaped states can self-trap in particular troughs. They are characterized by the total norm,

$$N = \int_0^{+\infty} r dr \int_0^{2\pi} d\theta |\Psi(r, \theta)|^2. \quad (5)$$

We look for stationary solutions to Eq. (3) which represent vortex QDs with chemical potential μ and integer WN S as

$$\Psi(r, \theta, t) = \psi(r) \exp(-i\mu t + iS\theta), \quad (6)$$

where $\psi(r)$ is a real radial wave function satisfying the equation

$$\mu\psi = -\frac{1}{2} \left(\frac{d^2\psi}{dr^2} + \frac{1}{r} \frac{d\psi}{dr} - \frac{S^2}{r^2} \psi \right) + V_0 \cos^2\left(\frac{\pi}{D}r\right) \psi + \ln(\psi^2) \cdot \psi^3. \quad (7)$$

Stationary vortex ring-shaped QDs, trapped in a radial potential trough labeled by number $O_n = 1, 2, 3, \dots$, as shown in Fig. 1(b), were produced by means of the imaginary-time-integration method [97, 98]. It was applied to an initial guess taken as

$$\Psi_0(r, \theta) = C \exp\left[-\alpha(r - r_n)^2 + iS\theta\right], \quad (8)$$

where C and $\alpha > 0$ are real numbers, and

$$r_n = (O_n - 1/2)D, \quad (9)$$

is the radial coordinate of the trough's bottom point. Then, the stability of the stationary QDs was analyzed by means of the linearized equations for perturbations with infinitesimal amplitude ε , which are introduced as

$$\Psi(r, \theta, t) = \left\{ \psi(r) + \varepsilon \left[u(r)e^{\gamma t + im\theta} + v^*(r)e^{\gamma^* t - im\theta} \right] \right\} e^{-i\mu t + iS\theta}, \quad (10)$$

where $u(r)$, $v(r)$, and γ are eigenmodes and the instability growth rate corresponding to an integer azimuthal index m of the perturbation, and $*$ stands for the complex conjugate. The linearization around the stationary solution leads to the system of the Bogoliubov – de Gennes equations,

$$\begin{pmatrix} F_{11} & F_{12} \\ F_{21} & F_{22} \end{pmatrix} \begin{pmatrix} u \\ v \end{pmatrix} = i\gamma \begin{pmatrix} u \\ v \end{pmatrix}, \quad (11)$$

where

$$\begin{aligned}
F_{11} &= -\frac{1}{2} \left[\frac{d^2}{dr^2} + \frac{d}{r dr} - \frac{(S+m)^2}{r^2} \right] + 2\psi^2 \ln(\psi^2) + \psi^2 + V(r) - \mu, \\
F_{12} &= \psi^2 \ln(\psi^2) + \psi^2, \\
F_{21} &= -\psi^2 \ln(\psi^2) - \psi^2, \\
F_{22} &= \frac{1}{2} \left[\frac{d^2}{dr^2} + \frac{1}{r} \frac{d}{dr} - \frac{(S-m)^2}{r^2} \right] - 2\psi^2 \ln(\psi^2) - \psi^2 - V(r) - \mu.
\end{aligned}$$

Numerical solutions of Eq. (11), obtained by means of the finite-difference method, produced a spectrum of eigenvalues γ , the stability condition being that the entire spectrum must be pure imaginary [99, 100]. Then, the stability of the stationary solutions was verified by direct simulations of the perturbed evolution in the framework of Eq. (3). The simulations were performed by means of the fast Fourier-transform method.

III. ANALYTICAL RESULTS: MODULATIONAL (IN)STABILITY OF NARROW VORTEX RINGS AND QUASI-1D SOLITONS

The fact that the 2D GP equation (3) gives rise to narrow vortex-ring modes populating particular circular troughs (see Fig. 3 below) suggests to approximate it by the 1D equation with the angular coordinate θ , while the radial coordinate r is eliminated. To this end, we adopt an approximate ansatz

$$\Psi(r, \theta, t) = \psi_0 \exp \left[-i \left(\chi + \frac{S^2}{2r_n^2} \right) t + iS\theta - \frac{(r-r_n)^2}{2w^2} \right] \psi(\tilde{\theta}, t), \quad (12)$$

with the 1D wave function $\psi(\tilde{\theta}, t)$, which is defined with respect to the rotating angular coordinate,

$$\tilde{\theta} = \theta - (S/r_n^2) t. \quad (13)$$

The radial center of ansatz (12) is pinned to $r = r_n$, where r_n is given by Eq. (9) and $w \ll D$ is a small radial thickness of the vortex ring, while constants ψ_0 and χ are defined below. To derive an effective 1D equation, ansatz (12) is substituted in Eq. (3), and the standard averaging procedure is applied, which implies the multiplication of the 2D equation by the same localization factor which is introduced in Eq. (12), i.e., $\exp\left(-\frac{(r-r_n)^2}{2w^2}\right)$, followed by the integration with respect to variable $(r-r_n)$ [101]. The result is

$$i \frac{\partial \psi}{\partial t} = -\frac{1}{2r_n^2} \frac{\partial^2 \psi}{\partial \tilde{\theta}^2} + \psi_0^2 \ln(|\psi|^2) \cdot |\psi|^2 \psi. \quad (14)$$

To cast the effective equation in this form, the constants in Eq. (12) are chosen as

$$\psi_0 = \exp\left(1/(8\sqrt{2})\right) \approx 1.092, \chi = 1/(2w)^2. \quad (15)$$

The CW (continuous-wave) solution of Eq. (14), with arbitrary constant amplitude a_0 , is

$$\psi = a_0 \exp[-i\psi_0^2 a_0^2 \ln(a_0^2) t]. \quad (16)$$

Because the sign of the nonlinearity in Eq. (14) is self-focusing at $|\psi|^2 < 1$ and defocusing at $|\psi|^2 > 1$, it is relevant to analyze the modulational instability of the CW state (16), which is a commonly known manifestation of the self-focusing [102]. To this end, Eq. (14) for the complex wave function ψ is replaced by coupled equations for the real amplitude and phase in the Madelung representation. Next, the equations are linearized for small perturbations $\sim \exp(im\tilde{\theta} + \gamma t)$, where m is an integer azimuthal index of the modulational perturbation, and γ is the respective instability growth rate, cf. Eq. (10). Then, a straightforward calculation yields

$$\gamma^2(m) = -\frac{m^2}{2r_n^2} \left[2\psi_0^2 a_0^2 \ln(ea_0^2) + \frac{m^2}{2r_n^2} \right]. \quad (17)$$

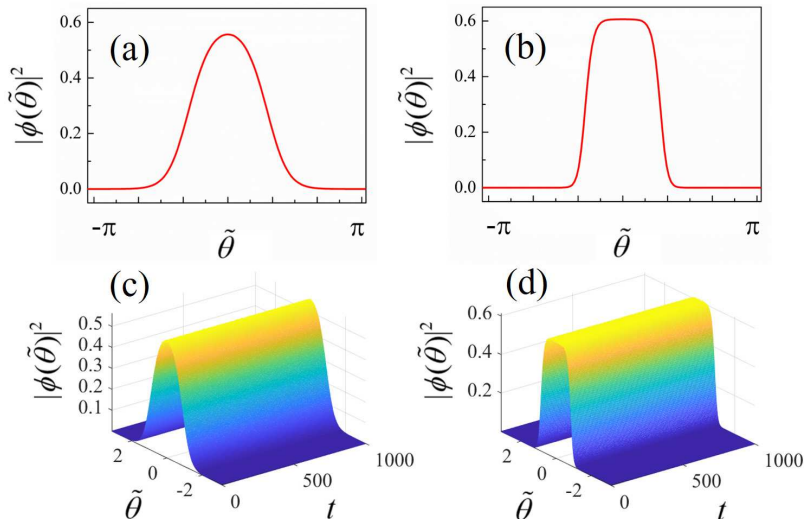


FIG. 2: (Color online) Typical examples of stable 1D solitons produced by Eq. (21). Panels (a) and (b) display, severally, density profiles of the solitons corresponding to $(N_{1D}, O_n) = (1,1)$ and $(N_{1D}, O_n) = (1,2)$, where N_{1D} is the 1D norm defined as per Eq. (22). (c,d) The perturbed evolution of the solitons shown in panel (a) and (b), produced by simulations of Eq. (14) with 1% random noise added to the input. Here, the radial period is $D = 6$.

The modulational instability (MI) occurs if Eq. (17) gives $\gamma^2 > 0$, the respective instability threshold being lowest for $m^2 = 1$,

$$a_0^2 \ln \left(\frac{1}{ea_0^2} \right) > \frac{1}{4\psi_0^2 r_n^2}. \quad (18)$$

On the contrary to the usual GP equation with cubic self-attraction, where the MI takes place if the CW amplitude is sufficiently high, Eq. (18) demonstrates that, in the presence of the logarithmic factor in Eq. (14), no MI arises if the ring's radius falls below the following minimum value:

$$r_n \leq e / (2\psi_0) \approx 1.244, \quad (19)$$

taking ψ_0 from Eq. (15).

If condition (18) holds, the MI transforms the CW into one or several strongly localized azimuthal (quasi-1D) solitons, which may perform rotary motion in the circular potential trough [77, 94, 95]. In this context, soliton solutions to Eq. (14) with chemical potential $\mu < 0$ are looked for as

$$\psi(\tilde{\theta}, t) = e^{-i\mu t} \phi(\tilde{\theta}), \quad (20)$$

where real function ϕ satisfies the equation

$$\mu\phi = -\frac{1}{2r_n^2} \frac{d^2\phi}{d\tilde{\theta}^2} + \psi_0^2 \ln(\phi^2) \cdot \phi^3. \quad (21)$$

Figure 2 displays typical examples of the 1D (azimuthal) soliton solutions, obtained by means of imaginary-time-integration method with periodic boundary conditions, which are characterized by values of the 1D norm,

$$N_{1D} = \int_0^{2\pi} \phi^2(\tilde{\theta}) d\tilde{\theta}. \quad (22)$$

These solutions are naturally feature spatial density profiles of two different types, *viz.*, bell-shaped and flat-top ones, see Figs. 2(a) and (b), respectively. The stability of these solitons is readily confirmed by direct simulations of their perturbed evolution, see Figs. 2(c,d).

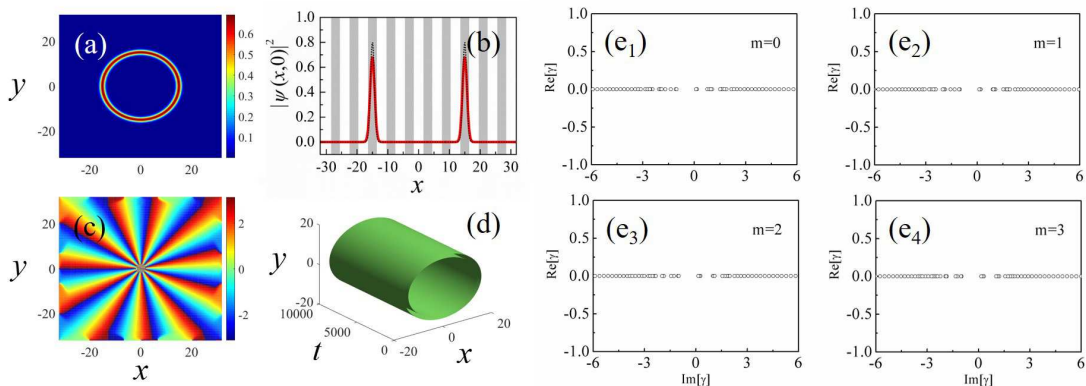


FIG. 3: (Color online) (a) A stable vortex ring-shaped QD with $S = 11$ and $O_n = 3$. The parameters are $N = 120$, $D = 6$ and $V_0 = 2$. (b) Its cross section along $y = 0$, $|\psi(x, 0)|^2$, is plotted by the red curves (the black dotted lines represent, for the comparison's sake, the result for $V_0 = 4$, other parameters remaining the same). (c) The phase pattern of the vortex ring. (d) Simulations of the perturbed evolution of the vortex ring shown in panel (a) with 1% random noise added to the input. (e₁-e₄): Perturbation eigenvalues for the same vortex ring, with azimuthal-perturbation indices $m = 0, 1, 2,$ and 3 , see Eq. (10).

Assuming that the soliton is narrow in comparison to the range of the variation of the angular coordinate, 2π , a straightforward corollary of Eq. (21) is a relation between the soliton's amplitude (maximum value), ϕ_0 , and μ :

$$\mu = \frac{\psi_0^2}{2} \phi_0^2 \left[\ln(\phi_0^2) - \frac{1}{2} \right]. \quad (23)$$

It is easy to see that Eq. (23) admits the existence of two distinct soliton families in a *finite band* of the values of μ ,

$$0 < -\mu < \psi_0^2 / (2\sqrt{e}) \equiv -\mu_{\min} \quad (24)$$

(the semi-infinite band $\mu < -\mu_{\min}$ remains empty, without any soliton population). As μ increases from μ_{\min} to -0 , one soliton family has its amplitude decreasing from $(\phi_0^2)_{\max} = 1/\sqrt{e}$ to 0. This family satisfies the Vakhitov-Kolokolov (VK) criterion, $dN_{1D}/d\tilde{\theta} < 0$, which is the well-known necessary stability condition for solitons created by any self-focusing nonlinearity [103–105]. The VK stability of this family is corroborated, in particular, by the corresponding dependence

$$N(\mu) \approx \frac{2}{r_n \psi_0^2} \frac{\sqrt{-2\mu}}{\ln(-1/\mu)}, \quad (25)$$

which is valid at $\mu \rightarrow -0$. The other, definitely unstable, soliton family, which does not satisfy the VK criterion, features the amplitude growing from $\phi_0^2 = 1/\sqrt{e}$ at $\mu = \mu_{\min}$ to $\phi_0^2 = \sqrt{e}$ at $\mu = -0$, in the same range of the variation of μ .

A majority of numerical results are reported below for the CW amplitudes of the ring vortices which have $a_0^2 \ln(1/ea_0^2) < 0$, hence the MI does not occur, according to Eq. (18). Nevertheless, we will also consider a nested pattern in which the inner (embedded) vortex ring is modulationally stable, while the MI occurs in the outer ring, giving rise to an azimuthal soliton orbiting around the inner ring. And vice versa: an azimuthal soliton may perform rotary motion in the inner trough, which is embedded in an outer trough filled by a modulationally stable vortex ring. Examples of such dynamical patterns are presented below in Fig. 11.

IV. NUMERICAL RESULTS

A typical example of a numerically constructed stable ring-shaped vortex QD with $S = 11$, trapped in the trough corresponding to $O_n = 3$ in Eq. (9), is displayed in Fig. 3, the other parameters being $N = 120$, $D = 6$ and $V_0 = 2$. It corresponds to the largest WN number, S_{\max} , which admits the stability for $O_n = 3$, as shown below in Fig. 9(b). The density cross section, $|\psi(x, 0)|^2$, which is displayed in Fig. 3(b), corroborates the placement of the vortex ring in the third potential trough. The stability of this QD is confirmed by direct simulations of its perturbed evolution and spectra of perturbation eigenvalues, as plotted in Figs. 3(d) and (e₁-e₄), respectively.

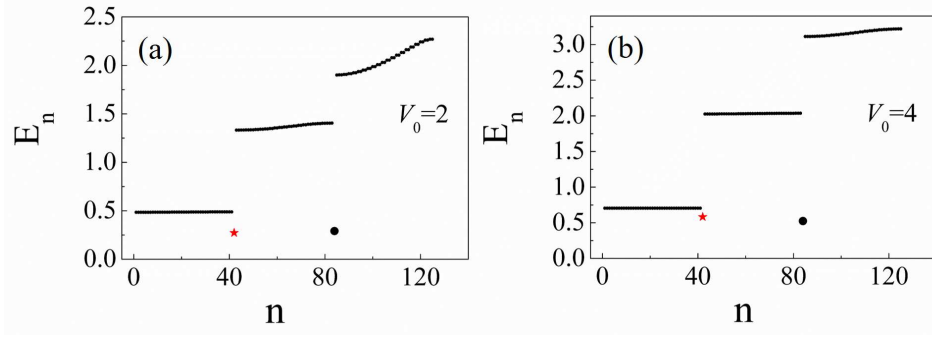


FIG. 4: (Color online) The black curves represent the energy levels E_n (eigenvalues of chemical potentials μ) corresponding to the lowest bands representing delocalized radial eigenstates produced by numerical solution of the linearized version of Eq. (7) with $V_0 = 2$ in (a) and $V_0 = 4$ in (b) in the limit of $r \rightarrow \infty$. Here n , attached to the horizontal axes, is the index of the eigenstates. Symbols \star and \bullet in (a) designate, respectively, values of μ for stable vortex-ring QDs with $S = 3$, $O_n = 3$, $N = 160$, and $S = 2$, $O_n = 2$, $N = 100$. In panel (b), the same symbols represent the ring-shaped QDs with $S = 1$, $O_n = 1$, $N = 30$, and $S = 4$, $O_n = 4$, $N = 200$, respectively. Here, the radial period of potential (4) is $D = 6$.

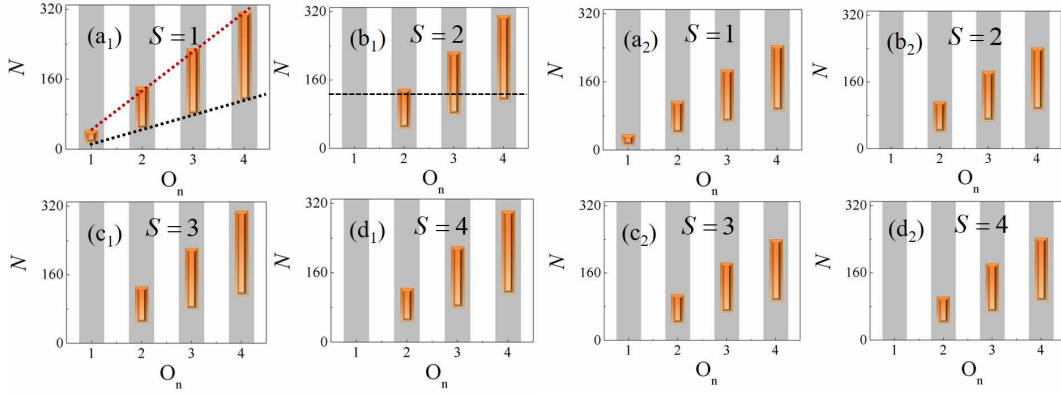


FIG. 5: (Color online) Orange bars represent stability intervals for the vortex ring-shaped QDs with $S = 1, 2, 3$ and 4 , which are placed in the radial-potential troughs with $O_n = 1, 2, 3$ and 4 [see Eq. (9)]. The red and black oblique dotted lines in panel (a₁) show the expansion of the stability area with the increase of O_n . The horizontal dashed line in panel (b₁) highlights the multistability, in the form of the coexistence of the vortex rings with the same norm but different values of O_n . The depth of the radial potential (4) is $V_0 = 2$ in panels (a₁-d₁) and $V_0 = 4$ in (a₂-d₂), while its radial period is $D = 6$.

It is relevant to calculate the bandgap spectrum of the linearized version of Eq. (7) with $r \rightarrow \infty$, and identify the position of the QD's eigenvalues μ with respect to the spectrum. Typical examples demonstrate in Fig. 4, for $V_0 = 2$ and 4 [see Eq. (4)], that the eigenvalues belong to the semi-infinite bandgap, located beneath all Bloch bands populated by delocalized radial eigenmodes. The same conclusion was made for other stable ring-shaped states.

Results of the numerical analysis of the stability of the vortex-ring QDs, with different WNs S , are summarized in Fig. 5 for different values of the radial-potential's depth V_0 [see Eq. (4)]. In the figure, the stability areas are shown by orange bars in the plane of norm N and radial-trough's number O_n , see Eq. (9). It is seen that, for fixed values of S and V_0 , the vortex rings are stable in a finite interval,

$$N_{\min} < N < N_{\max}. \quad (26)$$

At $N < N_{\min}$, the vortex QDs with the given parameters do not exist, while at $N > N_{\max}$ the peak (largest) density of the QDs essentially exceeds characteristic values $n \sim 1$ determined by the nonlinearity in Eq. (3), which leads to overfill of the given radial trough and filling adjacent troughs [see an examples in Fig. 7, in which the condensate fills two troughs]. The nonexistence of the QDs at $N < N_{\min}$ is explained by the fact that, for small values of N , the density falls to a value close to $n = 1$, at which the effective nonlinearity in Eq. (3), containing the logarithmic factor, vanishes, while the linear version of Eq. (3) with potential (4) cannot support any state localized in the radial direction.

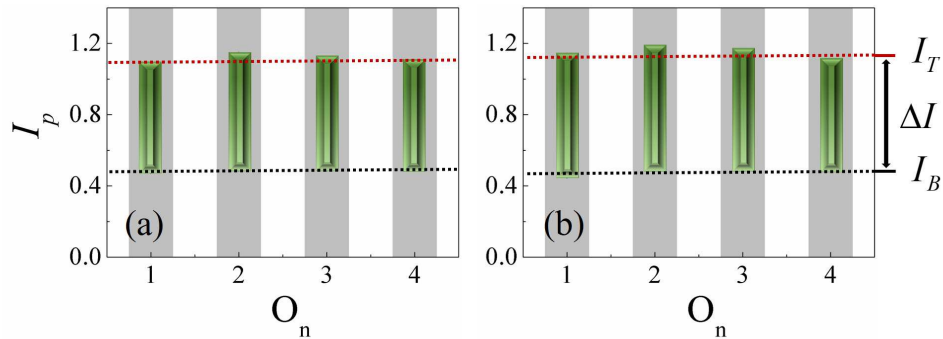


FIG. 6: (Color online) The peak density of the stable vortex ring-shaped QDs with $S = 1$, which are placed in the radial troughs with $O_n = 1, 2, 3$ and 4 . The parameters are $D = 6$ and $V_0 = 2$ in (a), or $V_0 = 4$ in (b). The numerical results yield $I_B \approx 0.48$, $I_T \approx 1.14$, and $\Delta I = I_T - I_B \approx 0.66$.

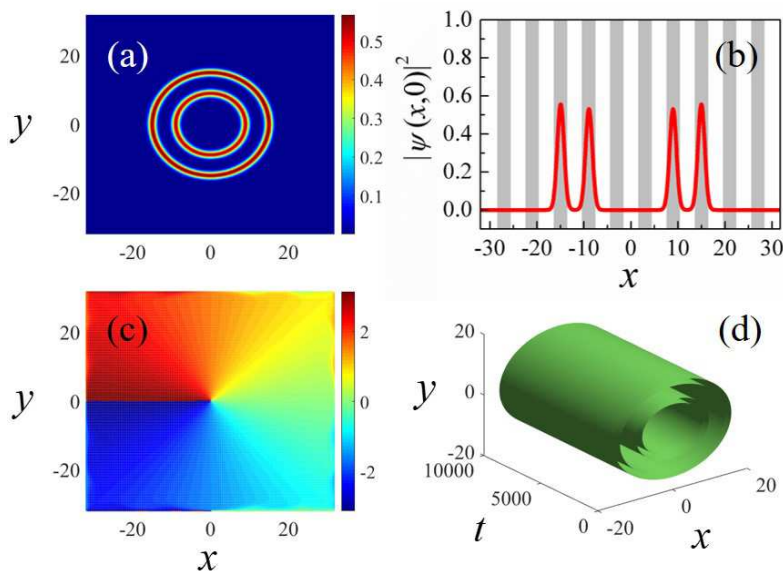


FIG. 7: (Color online) (a) An example of a stable ring-shaped vortex QDs with $S = 1$, which fills two radial troughs, with $O_n = 2$ and 3 . (b) Its cross section, $|\psi(x,0)|^2$, along $y = 0$. (c) The corresponding phase patterns. (d) Direct simulations of the perturbed evolution of the two-ring vortex QDs shown in panel (a) with 1% random noise added to the input. Here, the norm is $N = 150$, and other parameters are the same as in Fig. (3).

Note that the length of the stability interval in Fig. 5 increases with the growth of the trough's number, O_n . This trend can be explained as follows: according to Refs. [22, 92], vortex QDs are stable if their peak density takes values in a finite range around $n \sim 1$. To address this point in detail, green bars in Fig. 6 designate the peak density (I_p) of the stable vortex QDs with $S = 1$, which are placed in the radial troughs with numbers $O_n = 1, 2, 3$ and 4 . It is observed that I_p ranges between the bottom and top values, I_B and I_T (the black and red dotted lines, respectively, in Fig. 6). Further, the length of the narrow vortex ring is $l_n = 2\pi r_n = \pi(2O_n - 1)D$ [see Eq. (9)]. Thus, the boundaries of the stability interval (26) can be written as

$$\{N_{\min}, N_{\max}\} = \pi \{I_B, I_T\} (2O_n - 1)Dw/2, \quad (27)$$

where w , which depends on V_0 and D , is an effective width of the narrow QD in the radial direction, cf. Eq. (12). The respective width of the stability interval in Fig. 5 is

$$\Delta N = N_{\max} - N_{\min} = (\pi/2)\Delta I \cdot (2O_n - 1)Dw, \quad (28)$$

where $\Delta I = I_T - I_B$. Thus, the linear expansion of the stability interval with the increase of O_n is explained by Eq. (28).

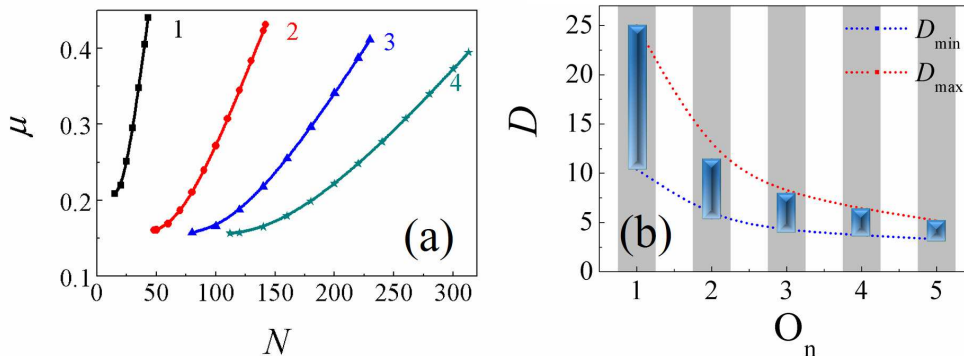


FIG. 8: (Color online) (a) The dependence of the chemical potential, μ , on norm, N , for the ring-shaped vortex QDs, which populate the radial troughs with $O_n = 1, 2, 3$ and 4, respectively. The parameters are the same as in Fig. 5(a₁). (b) The boundary values, D_{\min} and D_{\max} , of the period of the radial potential (4), between which the vortex rings are stable, for given values of O_n [see Eq. (29)]. The other parameters are $N = 120$, $V_0 = 2$, and $S = 1$.

Comparing the above results for $V_0 = 2$ [Figs. 5(a₁-d₁)] and $V_0 = 4$ [Figs. 5(a₂-d₂)], we conclude that the stability intervals are slightly longer in the former case. This finding can be explained too: the increase of the modulation depth of the potential, V_0 , causes slight decrease of the radial width w of the vortex rings [see the cross section $|\psi(x, 0)|^2$ in Fig. 3(b), where the red and black curves represent $V_0 = 2$ and $V_0 = 4$, respectively]. According to Eq. (28), this results in a decrease in ΔN .

If V_0 is fixed, the results reported in Ref. [25] demonstrate that the ring-shaped vortex QDs with a large topological charge tend to require a larger radius. For this reason, as shown in Fig. 5(b₁), the vortex ring with $S = 2$ cannot stably exist in the innermost radial trough corresponding to $O_n = 1$ in Eq. (9).

The present setting admits multistability of the vortex-ring QDs, as shown, in particular, by the horizontal dashed line in Fig. 5(b₁)). It highlights the coexistence of the stable vortex rings with equal norms, hosted by the radial troughs with different values of O_n but the same modulation depths.

Stable vortex QDs which fill more than one trough exist as well, see an example for $S = 1$ in Fig. 7. Actually, solutions of this type may be considered as an example of the concentric (nested) multi-ring vortex QDs, in the particular case when the coupled rings carry the same topological charge. Nested multi-ring complexes are considered in detail in the next section.

The dependence of the chemical potential, μ , of the ring-shaped vortex QDs on the total norm, N , is plotted in Fig. 8(a). The $\mu(N)$ curves in Fig. 8(a) feature a positive slope, $d\mu/dN > 0$, which contradicts the VK criterion. On the other hand, in the case of the effective self-repulsion in Eq. (3), which is the case for these solutions, the necessary stability condition for localized states is the *anti-VK* criterion, which is exactly $d\mu/dN > 0$ [82]. In the case of the sign-changing nonlinearity, such as that in Eq. (3), or the combination of cubic self-focusing and quintic defocusing in 1D [83] and 2D [84, 92] models, the necessary sign of the slope corresponding to stable localized states switches between $d\mu/dN < 0$ and $d\mu/dN > 0$.

Here, we provide an analysis to explain why the $\mu(N)$ curves for the vortex ring-shaped QDs obey the anti-VK criterion. We assume the value of the peak density of QDs is I_p , which can be estimated by $I_p \approx N/[\pi(2O_n - 1)Dw/2]$. According to Ref. [92], when $N > N_{\text{threshold}} = \pi(2O_n - 1)Dw/(2e)$, the anti-VK criterion, $d\mu/dN > 0$, is relevant as the necessary stability condition. In Fig. 8(a), the radial period is fixed as $D = 6$. If we select $w = D/2$, $N_{\text{threshold}}$ for $O_n = 1, 2, 3$ and 4 are $N_{\text{threshold}} \approx 10.4, 31.2, 52.0$ and 72.8, respectively. As shown in Fig. 8(a), the numerically found bottom stability boundaries for $O_n = 1, 2, 3$ and 4 are of $N_{\min} \approx 15, 48, 80$ and 112, respectively, which all are larger than $N_{\text{threshold}}$ for each value of O_n , hence the anti-VK criterion determines the stability in this case.

Multistability is also revealed by $\mu(N)$ curves Fig. 8(a). It is realized as the coexistence of vortex rings with equal values of the norm, trapped in the radial troughs with different values of O_n but the same potential depth V_0 .

The effect of the period of the radial potential, D , on the ring-shaped vortex QDs is presented in Fig. 8(b), where $N = 120$, $V_0 = 2$, and $S = 1$ are fixed. In this figure, the vortex ring are stable in intervals

$$D_{\min} < D < D_{\max}, \quad (29)$$

at given values of O_n . The fact that the length of the stability interval (29) decreases with the increase of O_n can be explained by dint of Eq. (27), which, for fixed N , yields

$$\Delta D \equiv D_{\max} - D_{\min} = \frac{N\Delta I}{\pi w(O_n - 1/2)I_B I_T}. \quad (30)$$

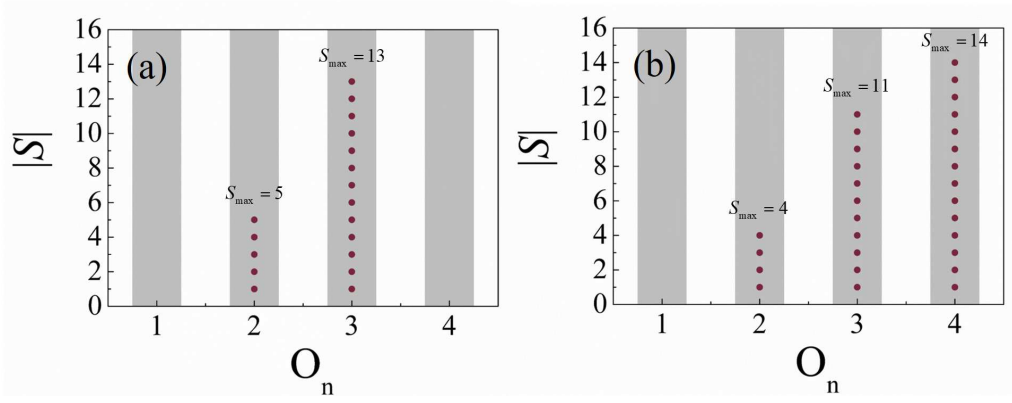


FIG. 9: (Color online) The trapping ability of the radial-potential troughs for the vortex rings with WN (winding number) $|S|$ versus O_n : (a) $N = 100$ and (b) $N = 120$. The other parameters are $D = 6$ and $V_0 = 2$.

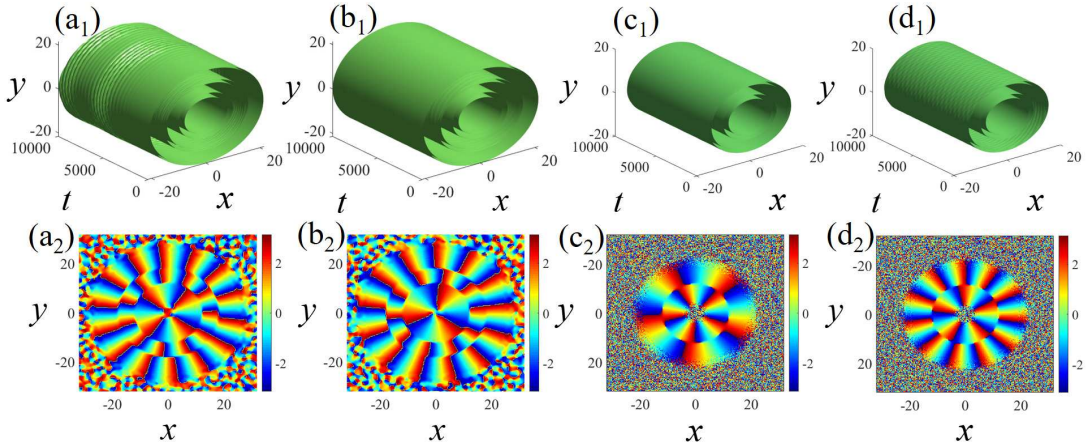


FIG. 10: (Color online) Typical examples of stable nested (multi-ring) vortex QDs. (a₁) A set of three rings characterized by $(N, S, O_n) = (120, 4, 2)$, $(120, 11, 3)$, and $(N, S, O_n) = (120, 14, 4)$. (b₁) The same, but with $(N, S, O_n) = (120, 3, 2)$, $(120, 10, 3)$, and $(N, S, O_n) = (120, 13, 4)$. (c₁) and (d₁) Typical examples of stable concentric two-ring vortex QDs with opposite signs of S in the coupled rings, whose parameters are $(N, S, O_n) = (100, 5, 2)$ and $(100, -5, 3)$, or $(100, 5, 2)$ and $(100, -11, 3)$, respectively. (a₂-d₂) Output phase patterns of the corresponding three- and two-ring states at $t = 10000$, which corroborates their structural stability. The other parameters are the same as in Fig. 9.

Note that the inverse proportionality of ΔD to $(O_n - 1/2)$, demonstrated by Eq. (30), agrees with the numerical findings presented in Fig. 8(b).

The ability of the radial potential (4) to maintain vortex rings with high values of S at different values of O_n , as produced by the numerical solution, is summarized in Figs. 9(a) and (b) for $N = 100$ and $N = 120$, respectively, while the other parameters are fixed, $D = 6$ and $V_0 = 2$. The results are consistent with those presented in Fig. 5(a₁). For these values of N , no stable solutions are found at $O_n = 1$, for instance, $N_{\max} = 43$ for $S = 1$ at $O_n = 1$, cf. Eq. 5. Similarly, no stable vortex rings with $N = 100$ exist in $O_n = 4$, because $N_{\min} = 112$ for $S = 1$ at $O_n = 4$. Generally, Fig. 9 shows that the holding capacity of the radial troughs increases with the growth of O_n . Comparison between Figs. 9(a) and (b) also reveals that the increase of the QD's norm reduces the capacity of the trough with given O_n .

V. MULTI-RING (NESTED) VORTEX QUANTUM DROPLETS

Typical examples of concentric multi-ring (nested) states are displayed in Fig. 10. Most interesting ones are the states composed of individual vortex rings with *different* WNs, cf. Ref. [96]. As generic examples of such states, Figs. 10(a₁) and (b₁) demonstrate robust three-ring solutions built of vortex rings with, respectively, $(N, S, O_n) = (120, 4, 2)$,

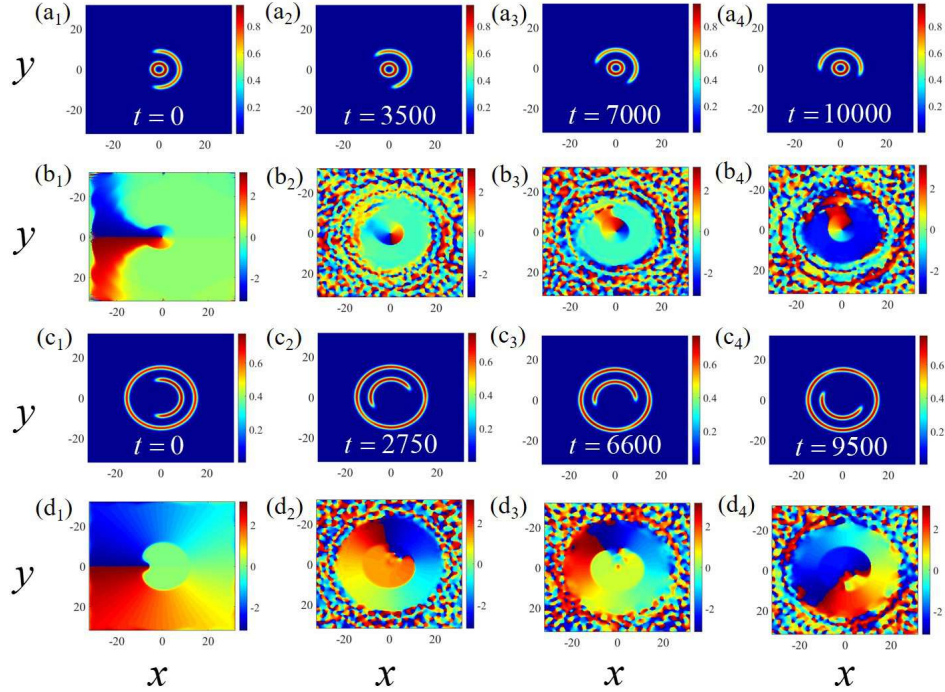


FIG. 11: (Color online) Typical examples of stable nested patterns with soliton and vortex QDs, which were created in adjacent radial troughs. In panels (a₁-b₄) the pattern was created from the initial dynamical states with parameters $(N, S, O_n) = (46, 0, 2)$ and $(N, S, O_n) = (35, 1, 1)$ in the outer and inner troughs, respectively. In panels (c₁-d₄) the input was taken with parameter sets $(N, S, O_n) = (120, 1, 3)$ and $(N, S, O_n) = (46, 0, 2)$ in the outer and inner troughs.

(120, 11, 3), and (120, 14, 4), or (120, 3, 2), (120, 10, 3), and (120, 13, 4). In direct simulations, such compound states remain stable for times exceeding $t = 10000$, which corresponds to ~ 300 diffraction times. These results offer a use in the design of encoding devices which employ winding numbers for the data storage.

It is worthy to note that it is also possible to construct stable concentric two-ring modes with *opposite signs* of S in the rings. This is somewhat similar to states with *hidden vorticity*, which are produced by a system of 2D GP equations including the self- and cross-component cubic nonlinear terms and the isotropic harmonic-oscillator potential trapping each component [53, 106]. Such states with vorticities $S = \pm 1$ in the two components have their stability region in the underlying parameter space. Typical examples of the stable concentric two-ring vortex QDs of this type, with parameters of the coupled rings $(N, S, O_n) = (100, 5, 2)$ and $(100, -5, 3)$, or $(100, 5, 2)$ and $(100, -11, 3)$, are displayed in Fig. 10(c₁) and (d₁), respectively. To confirm the stability of the three- and two-ring compound modes, Figs. 10(a₂-d₂) depict the respective output phase patterns at $t = 10000$.

As mentioned above, another noteworthy option is to construct a two-ring complex in which one vortex-ring component is subject to the MI, hence it is replaced by an azimuthal soliton (or maybe several solitons), see Eqs. (20) and (21), while the vortex component trapped in another potential trough avoids the azimuthal MI and remains essentially axisymmetric. Examples of such heterogeneous robust states, produced by simulations of Eq. (3), are displayed in Fig. 11. Panels 11(a₁-b₄) show a complex in which the MI takes place in the outer circular trough, producing an azimuthal soliton which performs rotary motion, while the inner vortex ring is modulationally stable. An opposite example is produced in Figs. 11(c₁-d₄), where the outer vortex ring remains stable against azimuthal perturbations, while the MI creates a soliton exhibiting the rotary motion in the embedded (inner) circular trough. The rotation direction of the soliton is driven by the vorticity sign of the underlying QD.

It is relevant to mention that the multi-ring potential considered here holds different vortex-ring or azimuthal-soliton states nearly isolating them from each other. In particular, this property offers the above-mentioned potential for the design of the data-storage device, in which different data components may be kept in different radial troughs. An additional problem, which is left for subsequent analysis, is interplay between adjacent radial modes in the case when the separation between the adjacent rings is essentially smaller.

VI. CONCLUSION

The subject of this work is the class of vortical ring-shaped QDs (quantum droplets) trapped in the 2D radially periodic potential. The underlying model is the GP equation with the cubic nonlinearity multiplied by the logarithmic factor, which represents the correction to the mean-field theory produced by quantum fluctuations. Effects of the depth and period of the potential on the vortex rings are studied, and their stability area is identified. Multistability of the vortex QDs is addressed too, demonstrating the coexistence of narrow vortex rings with equal norms in the radial-potential troughs with different radii. For the narrow rings, the 2D GP equation is approximately reduced to the 1D equation, which makes it possible to analyze the modulational stability of the rings against azimuthal perturbations. Multi-ring states in the form of nested patterns with different topological charges trapped in different radial troughs are found too. Also produced are robust dynamical states with modulationally stable narrow ring trapped in a particular circular trough, and an azimuthal soliton, created by the azimuthal modulational instability, in an adjacent trough. The results reported in this work suggest a new approach to the creation of stable QDs with embedded vorticity, which is a challenging problem. The results may also be used in the design of data-storage devices, with stable vortex rings trapped in different radial troughs used for encoding separate components of the data.

The present analysis can be extended in other directions. In particular, it may be interesting to generalize the model by considering an elliptically deformed radial potential. A challenging possibility is to extend the present analysis for three-dimensional settings.

VII. ACKNOWLEDGMENTS

This work was supported by NNSFC (China) through grant Nos. 11905032, 11874112, 11904051, Natural Science Foundation of Guangdong province through grant No. 2021A1515010214, the Guang Dong Basic and Applied Basic Research Foundation through grant No. 2021A1515111015, the Key Research Projects of General Colleges in Guangdong Province through grant No. 2019KZDXM001, the Special Funds for the Cultivation of Guangdong College Students Scientific and Technological Innovation through grant Nos. pdjh2021b0529, pdjh2022a0538, the Research Fund of Guangdong-Hong Kong-Macao Joint Laboratory for Intelligent Micro-Nano Optoelectronic Technology through grant No. 2020B1212030010, and Israel Science Foundation through grant No. 1695/22.

-
- [1] Petrov D S 2015 *Phys. Rev. Lett.* **115** 155302
 - [2] Petrov D S and Astrakharchik G E 2016 *Phys. Rev. Lett.* **117** 100401
 - [3] Schmitt M, Wenzel M, Böttcher F, Ferrier-Barbut I and Pfau T 2016 *Nature* **539** 259
 - [4] Chomaz L, Baier S, Petter D, Mark M J, Wächtler F, Santos L and Ferlaino F 2016 *Phys. Rev. X* **6** 041039
 - [5] Cabrera C R, Tanzi L, Sanz J, Naylor B, Thomas P, Cheiney P and Tarruell L 2018 *Science* **359** 301
 - [6] Cheiney P, Cabrera C R, Sanz J, Naylor B, Tanzi L and Tarruell L 2018 *Phys. Rev. Lett.* **120** 135301
 - [7] Semeghini G, Ferioli G, Masi L, Mazzinghi C, Wolswijk L, Minardi F, Modugno M, Modugno G, Inguscio M and Fattori M 2018 *Phys. Rev. Lett.* **120** 235301
 - [8] D’Errico C, Burchianti A, Prevedelli M, Salasnich L, Ancilotto F, Modugno M, Minardi F and Fort C 2019 *Phys. Rev. Research* **1**, 033155
 - [9] Lee T D, Huang K and Yang C N 1957 *Phys. Rev.* **106**, 1135
 - [10] Ilg T, Kumlin J, Santos L, Petrov D S and Buchler H P 2018 *Phys. Rev. A* **98** 051604(R)
 - [11] Zin P, Pylak M and Gajda M 2021 *Phys. Rev. A* **103** 013312
 - [12] Tylutki M, Astrakharchik G E, Malomed B A and Petrov D S 2020 *Phys. Rev. A* **101** 051601(R)
 - [13] Boudjemâa A 2018 *Phys. Rev. A* **98** 033612
 - [14] Hu H and Liu X 2020 *Phys. Rev. A* **102** 043302
 - [15] Pylak M, Gampel F, Płodzień M and Gajda M 2022 *Phys. Rev. Research* **4** 013168
 - [16] Parisi L and Giorgini S 2020 *Phys. Rev. A* **102** 023318
 - [17] Bisset R N, Peña Ardila L A and Santos L 2021 *Phys. Rev. Lett.* **126** 025301
 - [18] Kartashov Y V, Malomed B A and Torner L 2020 *Phys. Rev. Research* **2** 033522
 - [19] Otajonov S R, Tsoy E N and Abdullaev F K 2020 *Phys. Rev. E* **102** 062217
 - [20] Luo Z, Pang W, Liu B, Li Y and Malomed B A 2021 *Front. Phys.* **16** 32201
 - [21] Liu B, Zhang H, Zhong R, Zhang X, Qin X, Huang C, Li Y and Malomed B A 2019 *Phys. Rev. A* **99** 053602
 - [22] Zhao F, Yan Z, Cai X, Li C, Chen G, He H, Liu B and Li Y 2021 *Chaos Solitons and Fractals* **152** 111313
 - [23] Cui X 2018 *Phys. Rev. A* **98** 023630
 - [24] Ferrier-Barbut I, Wenzel M, Böttcher F, Langen T, Isoard M, Stringari S and Pfau T 2018 *Phys. Rev. Lett.* **120** 160402
 - [25] Lin Z, Xu X, Chen Z, Yan Z, Mai Zh and Liu B 2021 *Commun. Nonlinear Sci. Numer. Simulat.* **93**, 105536

- [26] Smith J C, Baillie D and Blakie P B 2021 *Phys. Rev. Lett.* **126** 025302
- [27] Hu H, Yu Z, Wang J and Liu X 2021 *Phys. Rev. A* **104** 043301
- [28] Lavoine L and Bourdel T 2021 *Phys. Rev. A* **103** 033312
- [29] Wang Y, Guo L, Yi S and Shi T 2020 *Phys. Rev. Research* **2** 043074
- [30] Dong L and Kartashov Y V 2021 *Phys. Rev. Lett.* **126** 244101
- [31] Guo Z, Jia F, Li L, Ma Y, Hutson J, Cui X and Wang D 2021 *Phys. Rev. Research* **3** 033247
- [32] Huang H, Wang H, Chen M, Lim C and Wong K 2022 *Chaos, Solitons and Fractals* **158** 112079
- [33] Guo M and Pfau T 2021 *Front. Phys.* **16** 32202
- [34] Malomed B A 2021 *Front. Phys.* **16** 22504
- [35] Xu S, Lei Y, Du J, Zhao Y, Hua R and Zeng J 2022 *Chaos, Solitons and Fractals* **164** 112665
- [36] Chen Y, Cai X, Liu B, Jiang X and Li Y 2022 *Acta Phys. Sin.* **71** 200302
- [37] Zhou Z, Shi Y, Ye F, Chen H, Tang S, Deng H and Zhong H 2022 *Nonlinear Dyn.* **110** 3769
- [38] Hu Y, Fei Y, Chen X and Zhang Y 2022 *Front. Phys.* **17** 6
- [39] Zhou Z, Shi Y, Tang S, Deng H, Wang H, He X and Zhong H 2021 *Chaos, Solitons and Fractals* **150** 111193
- [40] Kartashov Y V, Lashkin V M, Modugno M and Torner L 2022 *New J. Phys.* **24** 073012
- [41] Wang J, Hu H and Liu X J 2020 *New J. Phys.* **22** 103044
- [42] Boudjemâa A 2019 *New J. Phys.* **21** 093027
- [43] Rakshit D, Karpiuk T, Zin P, Brewczyk M, Lewenstein M and Gajda M 2019 *New J. Phys.* **21** 073027
- [44] Zin P, Pylak M and Gajda M 2021 *New J. Phys.* **23** 033022
- [45] Cikojević V, Markić L V and Boronat J 2020 *New J. Phys.* **22** 053045
- [46] Cidrim A, Salasnich L and Macrì T 2021 *New J. Phys.* **23** 023022
- [47] Karpiuk T, Gajda M and Brewczyk M 2020 *New J. Phys.* **22** 103025
- [48] Li Y Y, Luo Z H, Liu Y, Chen Z P, Huang C Q, Fu S H, Tan H S and Malomed B A 2017 *New J. Phys.* **19** 113043
- [49] Guebli N, and Boudjemâa A 2021 *Phys. Rev. A* **104** 023310
- [50] Boudjemâa A 2021 *Sci. Rep.* **11** 21765
- [51] Malomed B A 2022 *Multidimensional Solitons* (American Institute of Physics Publishing: Melville, NY)
- [52] Laburthe-Tolra B 2016 *Nature* **539** 276
- [53] Li Y, Chen Zh, Luo Zh, Huang Ch, Tan H, Pang W and Malomed B A 2018 *Phys. Rev. A* **98** 063602
- [54] Kartashov Y V, Malomed B A, Tarruell L and Torner L 2018 *Phys. Rev. A* **98** 013612
- [55] Malomed B A 2019 *Physica D* **399** 108-137
- [56] Zhang X, Xu X, Zheng Y, Chen Zh, Liu B, Huang Ch, Malomed B A and Li Y 2019 *Phys. Rev. Lett.* **123** 133901
- [57] Brazhnyi V A and Konotop V V 2004 *Mod. Phys. Lett. B* **18** 627-651
- [58] Morsch O and Oberthaler M 2006 *Rev. Mod. Phys.* **78** 179
- [59] Sakaguchi H and Malomed B A 2006 *Phys. Rev. E* **74** 026601
- [60] Baizakov B B, Malomed B A and Salerno M 2003 *Europhys. Lett.* **63** 642-648
- [61] Yang J and Musslimani Z H 2003 *Opt. Lett.* **28** 2094-2096
- [62] Sakaguchi H and Malomed B A 2005 *Europhys. Lett.* **72** 698-704
- [63] Zhang H, Chen F, Yu C, Sun L and Xu D 2017 *Chin. Phys. B* **26** 080304
- [64] Li Z, He P, Li L, Liang J and Liu W 2005 *Phys. Rev. A* **71** 053611
- [65] Zhu X, Li H, Shi Z, Xiang Y and He Y 2017 *J. Phys. B: At. Mol. Opt. Phys.* **50** 155004
- [66] Campbell R and Oppo G L 2016 *Phys. Rev. A* **94** 043626
- [67] Li F, Zong F and Wang Y 2013 *Chin. Phys. Lett.* **30** 060306
- [68] Chen Sh, Guo Q, Xu S, Belić M R, Zhao Y, Zhao D and He J 2019 *Appl. Math. Lett.* **92** 15
- [69] He Z, Zhang Z, Zhu Sh and Liu W 2014 *Acta Phys. Sin.* **63** 190502
- [70] Li Z and Li Q 2007 *Ann. Phys.* **322** 1961
- [71] Song Ch, Li J and Zong F 2012 *Chin. Phys. B* **21** 020306
- [72] Muñoz Mateo A, Delgado V, Guilleumas M, Mayol R and Brand J 2019 *Phys. Rev. A* **99** 023630
- [73] Zhao X, Zhang Y and Liu W 2019 *Acta Phys. Sin.* **68** 043703
- [74] Verma G, Rapo U D and Nath R 2017 *Phys. Rev. A* **95** 043618
- [75] Fan Z, Mai J, Chen Z, Xie M and Luo Z 2018 *Mod. Phys. Lett. B* **32** 1850070
- [76] Li H, Xu S, Belić M R and Cheng J 2018 *Phys. Rev. A* **98** 033827
- [77] Baizakov B B, Malomed B A and Salerno M 2006 *Phys. Rev. E* **74** 066615
- [78] Fetter A L 2001 *Phys. Rev. A* **64** 063608
- [79] Huang C, Zhong S, Li Ch and Dong L 2012 *Phys. Rev. A* **85** 063812
- [80] He Y, Malomed B A and Wang H 2007 *Phys. Rev. A* **76** 053601
- [81] Ye F, Kartashov Y V, Vysloukh V A and Torner L 2008 *Opt. Lett.* **33** 1288
- [82] Sakaguchi H and Malomed B A 2010 *Phys. Rev. A* **81** 013624
- [83] Merhasin I M, Gisin B V, Driben R and Malomed B A 2005 *Phys. Rev. E* **71** 016613
- [84] Driben R, Malomed B A, Gubeskys A and Zyss J 2007 *Phys. Rev. E* **76** 066604
- [85] Liu K, He H, Wang Ch, Chen Y and Zhang Y 2022 *Phys. Rev. A* **105** 013323
- [86] Ryu C, Andersen M F, Cladé P, Natarajan V, Helmerson K and Phillips W D 2007 *Phys. Rev. Lett.* **99** 260401
- [87] Kunimi M and Danshita I 2019 *Phys. Rev. A* **99** 043613
- [88] Yulin A V, Bludov Y V, Konotop V V, Kuzmiak V and Salerno M 2011 *Phys. Rev. A* **84** 063638
- [89] Roussou A, Smyrnakis J, Magiropoulos M, Efremidis N K and Kavoulakis G M 2017 *Phys. Rev. A* **95** 033606

- [90] Zhou Z, Yu X, Zou Y and Zhong H 2019 *Commun. Nonlinear Sci. Numer. Simulat.* **78** 104811
- [91] Dong L, Qi W, Peng P, Wang L, Zhou H and Huang Ch 2022 *Nonlinear Dyn.* **102** 303
- [92] Zheng Y, Chen S, Huang Z, Dai Sh, Liu B, Li Y and Wang Sh 2021 *Front. Phys.* **16** 22501
- [93] Huang C, Lyu L, Huang H, Chen Zh, Fu Sh, Tan H, Malomed B A and Li Y 2017 *Phys. Rev. A* **96** 053617
- [94] Kartashov Y V, Vysloukh V A and Torner L 2004 *Phys. Rev. Lett.* **93** 093904
- [95] Kartashov Y V, Vysloukh V A and Torner L 2005 *Phys. Rev. Lett.* **94** 043902
- [96] Aleksić B N, Aleksić N B, Skarka V and Belić M 2015 *Phys. Rev. A* **91** 043832
- [97] Chiofalo L M, Succi S and Tosi P M 2000 *Phys. Rev. E* **62**, 7438
- [98] Yang J and Lakoba T I 2008 *Stud. Appl. Math.* **120** 265
- [99] Mihalache D, Mazilu D, Malomed B A and Lederer F 2006 *Phys. Rev. A* **73** 043615
- [100] Dror N and Malomed B A 2011 *Physica D* **240** 526
- [101] Salasnich L, Parola A and Reatto L 2002 *Phys. Rev. A* **65** 043614
- [102] Agrawal G P 2013 *Nonlinear Fiber Optics* (Academic Press, Amsterdam)
- [103] Vakhitov N G and Kolokolov A A 1973 *Radiophys. Quantum Electron.* **16** 783-789
- [104] Bergé L 1998 *Phys. Rep.* **303** 259-370
- [105] Fibich G 2015 *The Nonlinear Schrödinger Equation: Singular Solutions and Optical Collapse* (Springer, Heidelberg)
- [106] Brtko M, Gammal A and Malomed B A 2010 *Phys. Rev. A* **82** 053610